Analysis of turbulent flow properties and energy fluxes in optimally controlled wind-farm boundary layers

2014 J. Phys.: Conf. Ser. 524 012178

(http://iopscience.iop.org/1742-6596/524/1/012178)

Analysis of turbulent flow properties and energy fluxes in optimally controlled wind-farm boundary layers

Jay P Goit and Johan Meyers

Department of Mechanical Engineering, KU Leuven, Celestijnenlaan 300, B3001 Leuven, Belgium

E-mail: jay.goit@kuleuven.be and johan.meyers@kuleuven.be

Abstract. In the present work our focus is to improve the performance of a wind farm by coordinated control of all turbines with the aim to increase the overall energy extraction by the farm. To this end, we couple flow simulations performed using Large Eddy Simulations (LES) with gradient based optimization to control individual turbines in a farm. The control parameters are the disk-based thrust coefficient of individual turbines as a function of time. They indirectly represent the effect of control actions that would correspond to blade-pitching of the turbines. We employ a receding-horizon predictive control setting and solve the optimization problem iteratively at each time horizon based on the gradient information obtained from the evolution of the flow field and the adjoint computation. We find that the extracted farm power increases by approximately 16% for a cost functional that is based on total energy extraction. However, this energy is gained from a slow deceleration of the boundary layer which is sustained for approximately 1 hour. We further analyze the turbulent stresses and compare to wind farms without optimal control.

1. Introduction

In large wind farms or 'deep arrays', the interaction of the wind farms with the planetary boundary layer plays a dominant role in a reduction of farm efficiency. For such cases, Calaf, Meneveau & Meyers[1], and Cal *et. al.*[2] demonstrated that the wind-farm energy extraction is dominated by the vertical turbulent transport of kinetic energy from higher regions in the boundary layer towards the turbine level. Later this was further corroborated in a series of studies, both relying on simulations [3, 4], as well as on wind-tunnel experiments [5, 6]. In the current study, we investigate the use of optimal control techniques combined with Large-Eddy Simulations (LES) of wind-farm boundary layer interactions for the increase of total energy extraction in very large wind farms. We consider the individual wind turbines as flow actuators, whose energy extraction can be dynamically regulated in time so as to optimally influence the flow field and the vertical turbulent energy transport, maximizing the wind farm power.

A lot of studies have considered optimization of wind-farm performance, many of them focussing on optimization of farm lay-out[7, 8]. Also farm control has received considerable attention, focussing on various aspects of wind-farm operation such as reduction of structural loads, power regulation, or increasing energy extraction [9, 10]. However, as far as wind-farm–flow interactions are included in these studies, they are all based on fast heuristic models: e.g.,

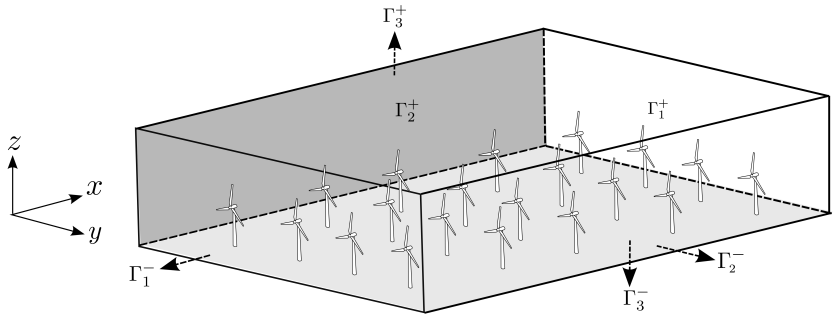

Figure 1: Computational domain Ω and boundaries Γ

models for wake interaction and merging such as presented by [11], or models for boundary-layer response in large farms [1]. In the current work, we consider the optimal control of wind farms using large-eddy simulations of the wind-farm boundary layer as the state model, allowing for a detailed optimization of the dynamic interaction of the farm's turbines with the boundary layer and its large-scale three-dimensional turbulent structures.

We employ a receding-horizon predictive control setting and iteratively solve an optimization problem at each time horizon based on the gradient information obtained from the evolution of flow field and adjoint computations. It is perhaps not very surprising that such algorithm is computationally demanding and therefore prohibitive for implementing directly as an online controller in a real wind farm. However, the results obtained with this approach allow us to identify the best possible performance of the controls for the turbines in the given farm layout and flow condition. This can act as a reference for future investigation into more practical models. We further discuss the various factors and constraints that should be taken into account to achieve the power gain in a large scale farm. Next to that, turbulent statistics are also analyzed and compared to wind farms without optimal control.

The paper is further organized as follows. We begin by presenting LES techniques used for wind-farm simulations. In section 3, we discuss the optimal control approach used in the current study, along with the adjoint method used for the derivation of the gradients. Results for the optimization case are discussed in section 4. Finally, in section 5 main conclusions and future research directions are presented.

2. Wind-farm boundary layer simulation

2.1. Numerical method

We consider thermally neutral pressure-driven boundary layer, with constant pressure gradient $\nabla p_\infty = f_\infty \boldsymbol{e}_1$. The governing equations are the filtered incompressible Navier-Stokes equations and the continuity equation, i.e.,

$$\nabla \cdot \widetilde{\boldsymbol{u}} = 0 \tag{1}$$

$$\frac{\partial \widetilde{\boldsymbol{u}}}{\partial t} + \widetilde{\boldsymbol{u}} \cdot \nabla \widetilde{\boldsymbol{u}} = -\frac{1}{\rho}\nabla \widetilde{p} + \frac{1}{\rho} f_\infty \boldsymbol{e}_1 + \nabla \cdot \boldsymbol{\tau}_M + \frac{1}{\rho}\boldsymbol{f} \tag{2}$$

where $\widetilde{\boldsymbol{u}}$ is the resolved velocity field, $\widetilde{p}$ the pressure field, $\boldsymbol{\tau}_M$ is the subgrid-scale model and $\boldsymbol{f}$ represents the forces introduced by the turbines on the flow.

The computational domain is schematically represented in figure 1. In stream-wise and span-wise directions, periodic boundary conditions are used. At the top boundary (Γ_3^+) symmetry conditions are imposed. The boundary condition imposed at the bottom surface comes from relating wall stresses $[\tau_{w1}, \tau_{w2}]$ to the wall-parallel velocity components $[\widetilde{u}_1, \widetilde{u}_2]$ at the first grid-point using Monin-Obukhov similarity theory [12], and is given by

$$\begin{aligned}\tau_{w1} &= -\left(\frac{\kappa}{\ln(z_1/z_0)}\right)^2 \left(\widetilde{\overline{u}}_1^2+\widetilde{\overline{u}}_2^2\right)^{0.5}\widetilde{\overline{u}}_1,\\ \tau_{w2} &= -\left(\frac{\kappa}{\ln(z_1/z_0)}\right)^2 \left(\widetilde{\overline{u}}_1^2+\widetilde{\overline{u}}_2^2\right)^{0.5}\widetilde{\overline{u}}_2,\end{aligned} \tag{3}$$

where z_0 is the surface roughness of the wall, and z_1 the vertical location of the first grid point. Furthermore, the bar on $\widetilde{\overline{u}}_1$ and $\widetilde{\overline{u}}_2$ represents a local average obtained by filtering the wall-parallel velocity in directions parallel to the wall, avoiding an overestimation of the wall stresses [13]. The subgrid-scale stresses are modelled with a standard Smagorinsky model [14], i.e.

$$\boldsymbol{\tau}_M = 2\ell^2(2\boldsymbol{S}:\boldsymbol{S})^{1/2}\boldsymbol{S}, \tag{4}$$

with $\boldsymbol{S} = (\nabla\overline{\boldsymbol{u}}+(\nabla\overline{\boldsymbol{u}})^T)/2$ the resolved rate-of-strain tensor. The Smagorinsky length ℓ ($= C_s\Delta$ far from the wall) is damped using Mason and Thomsons wall damping function [15] and we employ constant coefficient $C_s = 0.14$.

The turbine induced force $\boldsymbol{f}$ is based on the classical actuator-disk method which models the total thrust force acting on fluid due to the turbine and is written as,[1, 3, 16]

$$f^{(i)} = -\frac{1}{2}C'_{T,i}\rho\widehat{V}_i^2\mathscr{R}_i(\mathbf{x})\boldsymbol{e}_\perp, \tag{5}$$

with $C'_{T,i}$ the disk–based thrust coefficient and $\widehat{V}_i$ the average axial flow velocity at the turbine rotor disk. The disk-based thrust coefficient $C'_{T,i}$ results from integrated lift and drag coefficients over the turbine blades, taking design geometry and flow angles into account. Further, $\mathscr{R}_i(\mathbf{x})$ is a geometrical smoothing function, that distributes the uniform surface force of turbine i over surrounding LES grid cells. To this end, a Gaussian filter is used, leading to [16]

$$\mathscr{R}_i(\boldsymbol{x}) = \int_\Omega G(\boldsymbol{x}-\boldsymbol{x}')\,\delta[(\boldsymbol{x}'-\boldsymbol{x}_i)\cdot\boldsymbol{e}_\perp]\,\mathrm{H}(D/2-\|\boldsymbol{y}'\|)\,\mathrm{d}\boldsymbol{x}', \tag{6}$$

with $G(\boldsymbol{x}) = [6/(\pi\Delta_R^2)]^{3/2}\exp\left(-6\|\mathbf{x}\|^2/\Delta_R^2\right)$ the Gaussian filter kernel, with filter width Δ_R. Further $\boldsymbol{x}_i$ is the coordinate of the turbine rotor center, $\delta(x)$ the Dirac delta function, $\mathrm{H}(x)$ the Heaviside function, and where $\boldsymbol{y}' = (\boldsymbol{x}'-\boldsymbol{x}_i) - ((\boldsymbol{x}'-\boldsymbol{x}_i)\cdot\boldsymbol{e}_\perp)\boldsymbol{e}_\perp$ is the projection of $(\boldsymbol{x}'-\boldsymbol{x}_i)$ on the rotor plane. Similar to ealier studies [1, 3, 16], we select $\Delta_R = 3\Delta/2$, with Δ the LES grid resolution.

In order to determine the disk-averaged local velocity $\widehat{V}_i$, first spatial averaging is performed using the $\mathscr{R}_i(\boldsymbol{x})$, as a weighing factor,

$$V_i(t) = \frac{1}{A}\int_\Omega \widetilde{\boldsymbol{u}}(\boldsymbol{x},t)\cdot\mathbf{e}_\perp\,\mathscr{R}_i(\boldsymbol{x})\,\mathrm{d}\boldsymbol{x}, \tag{7}$$

with $A = \pi D^2/4$ the rotor–disk surface, and then $\widehat{V}_i$ is obtained from V_i using a first-order time filter, i.e.

$$\frac{\mathrm{d}\widehat{V}_i}{\mathrm{d}t} = \frac{1}{\tau}(V_i-\widehat{V}_i), \tag{8}$$

with τ the filter time scale. In the current study, we use τ =5 seconds. In our simulations, this ordinary differential equation is discretized using an implicit Euler method. Finally, the power that is extracted from the boundary layer by all turbines is expressed as

$$P = \int_\Omega \boldsymbol{f}\cdot\widetilde{\boldsymbol{u}}\mathrm{d}\boldsymbol{x} = \int_\Omega\sum_{i=1}^{N_t} -\frac{1}{2}C'_{T,i}\widehat{V}_i^2\,\widetilde{\boldsymbol{u}}\cdot\mathbf{e}_\perp\,\mathscr{R}(\boldsymbol{x})\,\mathrm{d}\boldsymbol{x}, \tag{9}$$

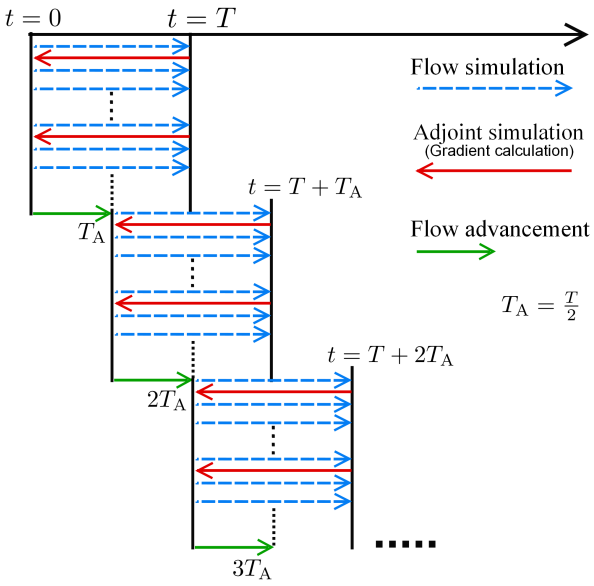

Figure 2: Receding horizon optimal control approach.

where N_t is the total number of turbines. This power is not equivalent to the power P_{ax} that is extracted at the turbine axle, which is related to the torque and rotational velocity of the turbine. The drag forces on the turbine blade increase the thrust force, but reduce the torque. Similar to $C'_{T,i}$ a disk-based power coefficient $C'_{P,i}$ may be defined that is based on projected forces in tangential direction. For the ideal case in absence of drag, $C'_{T,i} = C'_{P,i}$. In the current work, we focus on increasing P by controlling $C'_{T,i}$, and do not explicitly take $C'_{P,i}$ into account.

2.2. Discretization and Case setup

Simulations are performed in SP-Wind, an in-house research code that was developed in a series of earlier studies[1, 8, 16]. The code uses pseudo-spectral discretization techniques with the 3/2 de-aliasing of the convective and SGS terms in the horizontal directions. In the vertical direction a fourth-order energy-conservative finite difference discretization is used. Time advancement is performed using a four-stage fourth-order Runge-Kutta scheme. The time step is set to a fixed value of 0.7 seconds, which corresponds approximately to a CFL number of 0.4.

Simulations are performed on a mesh of $N_x \times N_y \times N_z = 256 \times 192 \times 81$ and a computational domain of size $L_x \times L_y \times H = 7.0 \times 3.0 \times 1$ (km^3). The farm consists of $N_\mathrm{t} = 50$ turbines, in a rectangular arrangement of 10×5. All 50 turbines are of same size with the rotor diameter $D = 100$ (m) and are assumed to have identical blade geometry as well as performance. The turbines are separated by $S_\mathrm{x} = 7D$ and $S_\mathrm{y} = 6D$ in x and y directions, respectively.

3. Optimization technique

As in any optimization problem, it is necessary to identify and define a cost functional appropriate for the problem of interest. Here we chose a cost functional that relates to

maximizing energy extraction. Thus

$$\begin{aligned}\mathscr{J} &= \int_0^T -P(t)\,\mathrm{d}t \\ &= \int_0^T \int_\Omega \sum_{i=1}^{N_t} -\frac{1}{2} C'_{\mathrm{T,i}} \widehat{V}_i^2\, \mathscr{R}_i(\boldsymbol{x}) \boldsymbol{u}(\boldsymbol{x},t)\cdot\mathbf{e}_\perp \,\mathrm{d}\boldsymbol{x}\,\mathrm{d}t. \end{aligned} \tag{10}$$

The control parameters are the turbine thrust coefficients $C'_{\mathrm{T,i}}$. These are parameters that represent the effects of changing the blade pitch of the turbines either capturing more or less of the available energy in the wind.

We employ a receding-horizon model predictive control technique for the control of wind-farm boundary layer interaction. A similar setting is employed by Bewley *et al.*[17] in the context of drag reduction. In a receding-horizon optimal control approach, time is split in a number of control windows with length T, also called the time horizon – a schematic overview is presented in figure 2. Staring with the first time horizon, an optimization problem is formulated in which the control parameters are optimized as function of time. To that end, an iterative, gradient-based optimization approach is used requiring several large-eddy simulations, combined with adjoint simulations for the determination of the gradients. Once a set of optimal controls is found for the interval $[0, T]$, they are effectively used as control inputs to advance the system over a time window T_A (see Figure 2). Subsequently, a new optimization problem is formulated that optimizes the controls for the time window $[T_A, T_A + T]$, and so forth. One of the constraints in the current frame work is the periodic boundary condition in streamwise direction, which means T should be smaller than through-flow time so that the influence of periodicity on the optimization is avoided. We choose T to be the time taken by the flow to cross four turbines in a row and flow advancement time $T_A = T/2$.

The control $C'_{\mathrm{T,i}}(t)$ for the particular optimization horizon is improved iteratively using the relation

$$C'^{(k+1)}_{\mathrm{T,i}} = C'^{(k)}_{\mathrm{T,i}} + \alpha\, \delta C'^{(k)}_{\mathrm{T,i}}, \tag{11}$$

where $\delta C'^{(k)}_{\mathrm{T,i}}$ is the search direction, α is the step length and k is the iteration number. The search direction $\delta C'^{(k)}_{\mathrm{T,i}}$ is determined using efficient Polak-Ribiére conjugate-gradient method which depends on the gradient of the cost functional $\nabla\mathscr{J}$ and the search direction from previous step. The optimum value for the step length, α along the search direction is computed using an iterative line search method based on mnbrak and Brent algorithms [18]. For details about the line search algorithm used in this study, reader is referred to Delport *et al.*[19, 20].

Next, we briefly explain the adjoint equations which should be solved for the gradient evaluation. We employ a formal Lagrangian method for the derivation of adjoint equations. A similar method is presented by Choi *et al.*[21]. For every state variables ($\widetilde{\boldsymbol{u}}$, $\widetilde{p}$, $\widehat{\boldsymbol{V}}$), also known as primal variables, an adjoint variable ($\widetilde{\boldsymbol{\xi}}$, $\widetilde{\pi}$, χ) is associated. These adjoint variables also act as the Lagrange multipliers. We associate following Lagrangian function to our optimization problem.

$$\begin{aligned}\mathscr{L} = \mathscr{J} &+ \int_0^T \int_\Omega \left[\frac{\partial \widetilde{\boldsymbol{u}}}{\partial t} + \widetilde{\boldsymbol{u}}\cdot\nabla\widetilde{\boldsymbol{u}} + \frac{1}{\rho}\nabla\widetilde{p} + \nabla\cdot\tau_M - \frac{1}{\rho}\boldsymbol{f} - \tau_{w,i}\delta(z)\right]\cdot\widetilde{\boldsymbol{\xi}}\; d\Omega\; dt \\ &- \int_0^T \int_\Omega \widetilde{\pi}\cdot\mathrm{div}\;\widetilde{\boldsymbol{u}}\; d\Omega\; dt + \int_0^T \sum_{i=1}^{N_t}\left[\sigma\frac{\mathrm{d}\widehat{\boldsymbol{V}}}{\mathrm{d}t} - (\boldsymbol{V} - \widehat{\boldsymbol{V}})\right]\cdot\chi\; dt \end{aligned} \tag{12}$$

For the optimal condition, we expect that the partial derivatives of $\mathscr{L}$ with respect to the state variables ($\widetilde{\boldsymbol{u}}$, $\widetilde{p}$, $\widehat{\boldsymbol{V}}$) are zero, i.e.,

$$\mathscr{L}_{\widetilde{p}}(\delta\widetilde{p}) = 0, \quad \mathscr{L}_{\widetilde{\boldsymbol{u}}}(\delta\widetilde{\boldsymbol{u}}) = 0, \quad \mathscr{L}_{\widehat{\boldsymbol{V}}}(\delta\widehat{\boldsymbol{V}}) = 0, \tag{13}$$

where $\delta\widetilde{p}$, $\delta\widetilde{\boldsymbol{u}}$ and $\delta\widehat{\boldsymbol{V}}$ are the directions in which derivatives are taken. Substituting from the definition of Lagrangian of Eq. (12) and performing integration by parts in Eq. (13) leads to a set of adjoint equations:

$$
\begin{aligned}
&-\frac{\partial\widetilde{\boldsymbol{\xi}}}{\partial t}-\widetilde{\boldsymbol{u}}\cdot\nabla\widetilde{\boldsymbol{\xi}}-(\nabla\widetilde{\boldsymbol{\xi}})^T\cdot\widetilde{\boldsymbol{u}}=-\frac{1}{\rho}\nabla\widetilde{\pi}-\nabla\cdot\boldsymbol{\tau}^*_M+\frac{1}{\rho}\boldsymbol{f}^*+\delta(z)(\tau^*_{w1}\boldsymbol{e}_1+\tau^*_{w2}\boldsymbol{e}_2)\\
&\nabla\cdot\widetilde{\boldsymbol{\xi}}=0\\
&-\frac{\mathrm{d}\chi_i}{\mathrm{d}t}=\frac{1}{\tau}\left[-\chi_i+C'_{T,i}\widehat{V}_i\int_\Omega\mathscr{R}_i(\mathbf{x})\;(\widetilde{\boldsymbol{u}}-\widetilde{\boldsymbol{\xi}})\cdot\boldsymbol{e}_\perp\,\mathrm{d}\boldsymbol{x}\right],\qquad\text{for}\;\;i=1\cdots N_t,
\end{aligned}
\tag{14}
$$

and with

$$
\boldsymbol{f}^*=\sum_{i=1}^{N_t}\left(\frac{1}{2}C'_{T,i}\widehat{V}_i^2+\frac{\chi_i}{A}\right)\mathscr{R}_i(\boldsymbol{x})\boldsymbol{e}_\perp,
\tag{15}
$$

$$
\tau^*_{w,i}=-\left[\frac{\kappa}{\log(z_1/z_0)}\right]^2\overline{\left\{\left(\overline{\widetilde{u}}_1^2+\overline{\widetilde{u}}_2^2\right)^{1/2}\xi_i+\frac{\overline{\widetilde{u}}_1\xi_1+\overline{\widetilde{u}}_2\xi_2}{\left(\overline{\widetilde{u}}_1^2+\overline{\widetilde{u}}_2^2\right)^{1/2}}\overline{\widetilde{u}}_i\right\}},\qquad\text{for}\;\;i=1,2,
\tag{16}
$$

Further

$$
\boldsymbol{\tau}^*_M=2\ell_s^2\left(\frac{2\boldsymbol{S}:\boldsymbol{S}^*}{(2\boldsymbol{S}:\boldsymbol{S})^{1/2}}\boldsymbol{S}+(2\boldsymbol{S}:\boldsymbol{S})^{1/2}\boldsymbol{S}^*\right),
\tag{17}
$$

where $\boldsymbol{S}^*=(\nabla\boldsymbol{\xi}+(\nabla\boldsymbol{\xi})^T)/2$.

The spatial boundary conditions of the adjoint equations are equivalent to those of the forward equations. In x_1, and x_2 directions periodic boundary conditions are required. In the normal direction symmetry boundary conditions is required at the top wall and impermeability at bottom wall. For the 'initial conditions', it is important to realize that the adjoint equations are solved backward in time (cf. the sign of the time derivatives).

Finally, let us close this section by defining the gradient of the cost functional. The sensitivity of the cost functional can be computed from the partial derivative of $\mathscr{L}$ with respect to the control parameter [22] $C'_{\mathrm{T,i}}$ and it corresponds to

$$
\nabla\mathscr{J}=\int_0^T\int_\Omega\sum_{i=1}^{N_t}\frac{1}{2}\overline{V}_n^2\left\{-V_n+\widetilde{\xi}\right\}\;\mathscr{R}_{1,\mathrm{n}}(\mathbf{x})\;d\Omega\;dt.
\tag{18}
$$

4. Optimally controlled wind farm

4.1. Power output and energy balance

In figure 3, snapshots of the instantaneous velocity and adjoint fields are shown. From the velocity field countour, we observe significant meandering of the turbine wakes. At the same time patches of high speed wind can also be seen passing through the spaces between turbine columns. Unlike the flow field, the adjoint fields evolves backward in time, and propagates in the upstream direction. It grows gradually backward in time, and becomes turbulent, when fully developed.

Figure 4 shows the behavior of the thrust coefficient for one of the turbines in the controlled wind farm. Approximately 1h of time is shown. We observe strong changes in C'_T in response to the turbulent flow field. Note that in the control, the lower and upper limit for the C'_T are

(a) (b)

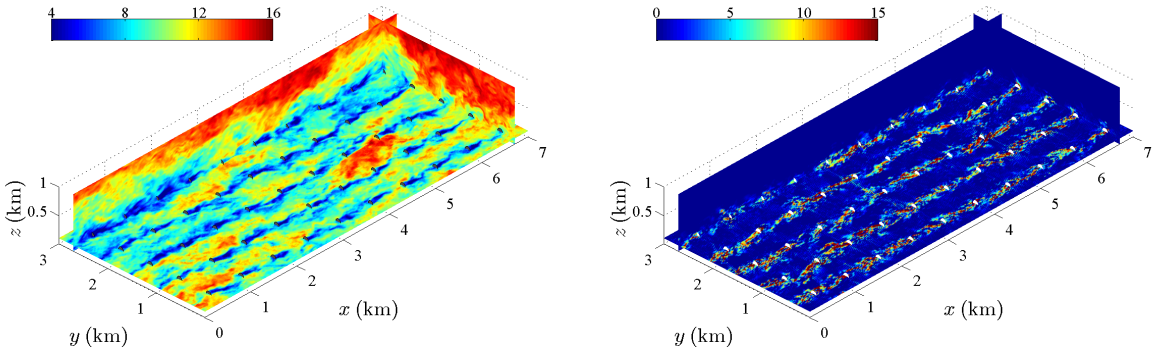

Figure 3: Contours of instantaneous field. (a) Streamwise velocity field, (b) Streamwise component of adjoint field at time $T - t = 126$ seconds. Horizontal planes in the figures are taken at the hub height.

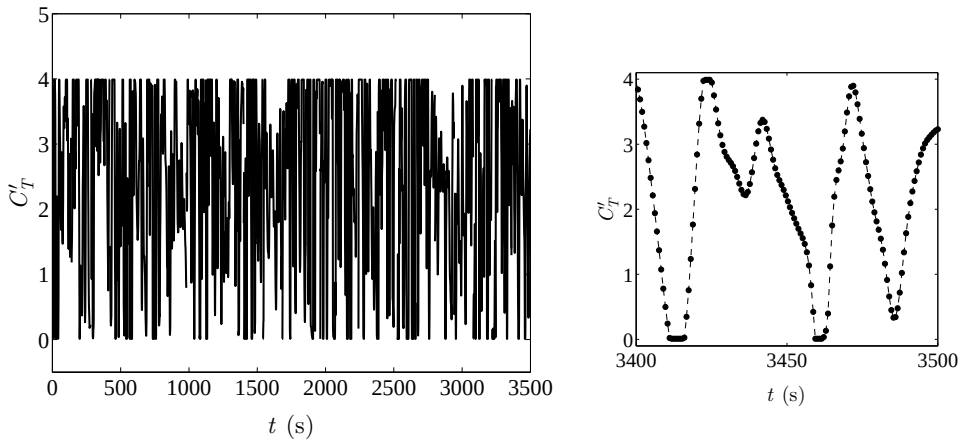

Figure 4: Time evolution of the thrust coefficient of one of the turbines in the farm.

set respectively to 0 and 4 using a box constraints. This is necessary, because if left entirely to the controller, it may designate a very high or even a negative value to the thrust coefficient, as long as optimized power output is achieved. However, turbines with very large C_T' may not be feasible, also negative C_T' means the turbine is pumping energy into the boundary layer. For the upper limit, first we investigate how C_T' relates to several design parameters such as the turbine blade chord and the operational tip-speed ratio for a real turbine. We consider the specification of the "NREL offshore 5-MW baseline wind turbine" [23] as a reference case and compute C_T' for a range of parameters. Based on this calculation we choose a maximum value for C_T' of 4. The time series of C_T' may seem to be very random, but when further zoomed in, we observe that it evolves smoothly, and is well resolved by the discretization; no additional smoothing of the gradients used in the optimization was required for this.

Figure 5 (a) shows the time series of the total instantaneous power extracted from the farm. It is obvious from the figure that there is an increase in power extraction when the controller is

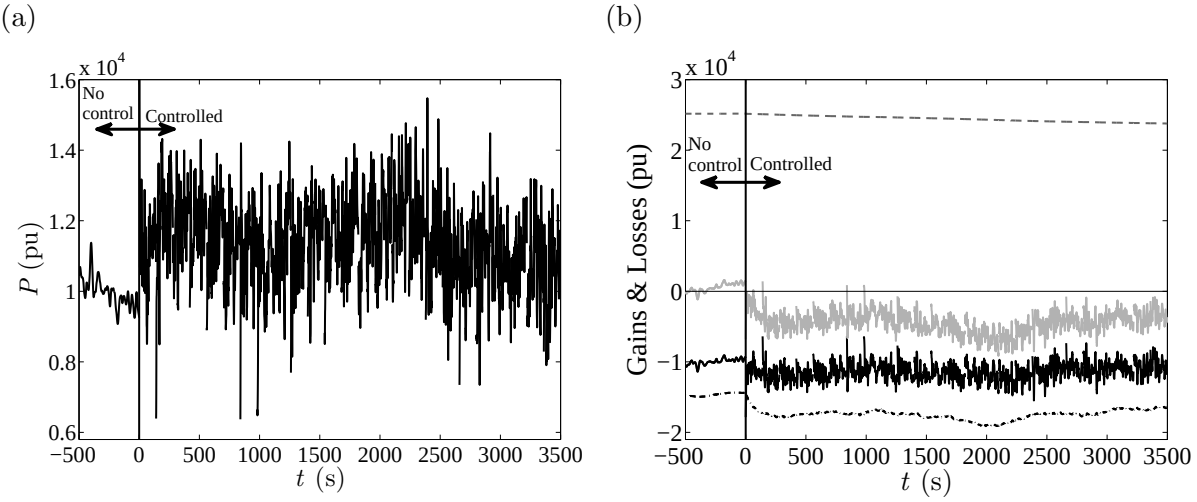

Figure 5: Time evolution of (a) total farm power output, (b) gains and losses. Dashed line: driving pressure force; grey line: rate of change of kinetic energy; dark line: farm power; dot dashed line: dissipation.

active. This instantaneous power when integrated over time according to

$$P_{\text{tot}} = \int_{n\,T_{\text{A}}}^{(n+1)\,T_{\text{A}}} \sum_{i=1}^{N_t} -P_i \; dt, \tag{19}$$

where $n = 0, 1, 2....$, we find that on average there is 16% gain in the total power as a result of the optimization. We further evaluate gains and losses in terms of the instantaneous kinetic energy equation, in figure 5(b). The balance of kinetic energy, obtained from the NS equation Eq. (2), may be written as

$$\frac{\mathrm{d}}{\mathrm{d}t}\int_{\Omega} E d\Omega = \int_{\Omega} f_{\infty}\widetilde{u} d\Omega - \sum_{i=1}^{N_t} P_i - \int_{\Omega} \mathscr{D} d\Omega. \tag{20}$$

where E is the kinetic energy of the flow and $\mathscr{D}$ is a turbulent dissipation. The external energy input in the boundary layer driven by the pressure gradient remains almost constant. While the optimization increases the extracted power, it is also responsible for a significant increase in the loss to the dissipation (dot dashed line). As a consequence, the flow in the boundary layer slows down resulting in a negative rate of kinetic energy. It may be conceivable that a slowdown of the boundary layer is not a problem, so long as it leads to a gain in the power, but in that case the transient flow condition persists throughout the simulation. To achieve a new regime of steady state during the optimization, it may be necessary to redefine the objective function, e.g. by penalizing the boundary-layer deceleration. Nevertheless, also the transient regime found in the current study may be of interest. In particular, an increased energy extraction (16%) for a time period of 1 hour may be relevant for grid support.

4.2. Turbulence statistics

Figure 6 shows the streamwise components of the mean velocity profiles, both with and without optimal control. We observe, that the profiles are strongly affected by the presence of the controller, slowing down the flow. For the earlier optimal-control windows, the slow down is

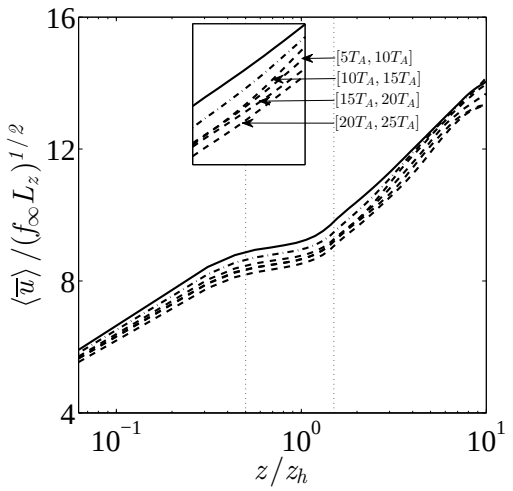

Figure 6: Streamwise mean velocities. Uncontrolled case (—). The optimal control case is averaged over the time window: $[0, 5T_A]$ (-·-·-); higher time windows (- - -).

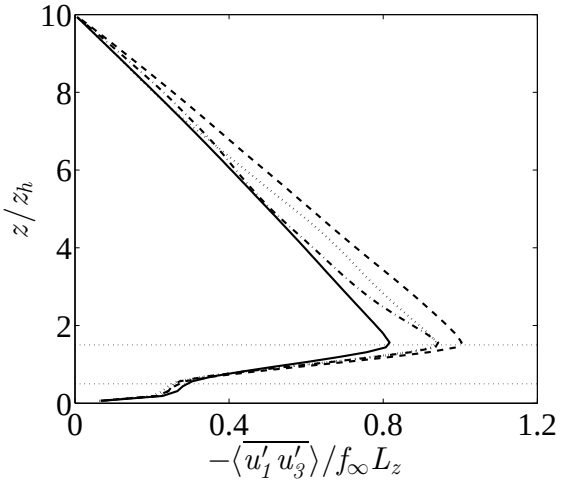

Figure 7: Vertical profiles of shear stresses. Uncontrolled case (—). The optimal control case averaged over time window $[0, 5T_A]$ (-·-·-); time window $[5T_A, 20T_A]$ (- - -) and time window $[20T_A, 25T_A]$ (····).

more obvious in the bottom half of the domain. At the later windows, there is not much slow down in the disc region, whereas, the upper part of the domain experiences a more pronounced deceleration. Thus it may be reasonable to assume that the flow is in locally equilibrium in the lower half, especially in the disc region.

In figure 7, the shear stresses profiles for the optimization case are compared with the uncontrolled simulation. For both controlled and uncontrolled cases, the shear stresses increase in the rotor region, and reach a maximum value near the top of the wind turbines. The shear stress in the disk region is significantly higher for the controlled case than the uncontrolled case. Furthermore, in the earlier part of the simulation, a gradual increase in the shear stress is observed, but it decreases at the later time. A similar trend is visible also in the farm power output in the later part of the simulation, when the gain is not as high as earlier phase.

5. Conclusion

The present paper discusses the implementation of the gradient based optimization technique for the power optimization of a large scale wind farm. We present the formal derivation of the adjoint equations necessary for gradient calculation. Optimization is performed in the LES - based receding horizon framework, in which control C_T' is optimized over the fixed time horizon, before advancing forward to the next iteration.

Optimal control result demonstrates that for the current cost functional definition, gain in the total power output with respect to the uncontrolled case is about 16%. However, this increase in the extracted power is related to a deceleration of the boundary layer, at the same time increasing the turbulent dissipation. No new statistical equilibrium was found yet, though also the transient regime identified in the current work, with an increased energy extraction that is sustained for a period of approximately 1 hour may be interesting from a practical point of view for, e.g., balancing total power demand of the utility grid and assisting in the grid frequency regulation. Analysis of the turbulence statistics show significant increase in the shear stress for the controlled case. Further research focusses on the redefinition of the objective function and identification of a statistical equilibrium and the potential gains in such a regime.

Acknowledgments
The authors acknowledge support from the European Research Council (FP7–Ideas, grant no. 306471) the Research Foundation – Flanders (FWO, grant no. G.0376.12). Simulations were performed on the computing infrastructure of the VSC (Flemish Supercomputer Center), funded by the Hercules foundation.

References

[1] Calaf M, Meneveau C and Meyers J 2010 *Phys. Fluids* **22** Art no 015110. DOI: 10.1063/1.3291077

[2] Cal R B, Lebron J L, Castillo L, Kang H S and Meneveau C 2010 *J. Ren. and Sust. Energy* **2** 013106

[3] Meyers J and Meneveau C 2013 *Journal of Fluid Mechanics* **715** 335–358

[4] Abkar M and Porté-Agel F 2013 *Energies* **6**(5) 2338–2361

[5] Chamorro L P, Arndt R E A and Sotiropoulos F 2011 *Boundary-Layer Meteorology* **141**(3) 349–367

[6] Newman J, Lebron J, Meneveau C and Castillo L 2013 *Physics of Fluids* **25**

[7] Newman B G 1976 *Energy Conv.* **16** 169–179

[8] Meyers J and Meneveau C 2012 *Wind Energy* **15** 305–317

[9] Soleimanzadeh M, Wisniewski R and Kanev S 2012 *J. Wind Eng. Ind. Aerodyn.* **107-108** 256–262

[10] Fleming P, Gebraad P, Lee S, Churchfield M, Scholbrock A, Michalakes J, Johnson K and Moriarty P 2013 *Proc. EWEA 2013, 4-7 February 2013, Vienna, Austria* **EWEA** 1–12

[11] Rathmann O, Frandsen S and Barthelmie R 2007 *European Wind Energy Conference and Exhibition* (Milan, Italy) p BL3.199

[12] Moeng C H 1984 *J. Atmos. Sci.* **41** 2052–2062

[13] Bou-Zeid E, Meneveau C and Parlange M B 2005 *Physics of Fluids* **17**

[14] Smagorinsky J 1963 *Monthly Weather Review* **91** 99–165

[15] Mason P J and Thomson T J 1992 *Journal of Fluid Mechanics* **242** 51–78

[16] Meyers J and Meneveau C 2010 *48th AIAA Aerospace Sciences Meeting Including the New Horizons Forum and Aerospace Exposition, Orlando, Florida* **AIAA 2010-827** 1–10

[17] Bewley T R, Moin P and Temam R 2001 *J. Fluid Mech.* **447** 179–225

[18] Press W H, Teukolsky S A, Vetterling W T and Flannery B P 1996 *Numerical Recipes in FORTRAN77: The art of scientific computing* (Cambridge University Press, 2nd edition)

[19] Delport S, Baelmans M and Meyers J 2009 *J. Turbul.* **10** 18

[20] Delport S, Baelmans M and Meyers J 2011 *Phys. Fluids* **25** 045105

[21] Choi H, Hinze M and Kunisch K 1999 *Applied Numerical Mathematics* **31** 133 – 158

[22] Borzi A and Schultz V 2012 *Computational optimization of systems governed by partial differential equations* (Philadelphia: SIAM)

[23] Jonkman J, Butterfield S, Musial W and Scott G 2009 Definition of a 5-mw reference wind turbine for offshore system development Tech. Rep. NREL/TP-500-38060 National Renewable Energy Laboratory Cole Boulevard, Golden, Colorado